CHEMISTRY
A EUROPEAN JOURNAL

DOI: 10.1002/chem.201000661

Cobalt Coordination and Clustering in α-$Co(OH)_2$ Revealed by Synchrotron X-ray Total Scattering

James R. Neilson,[a] Joshua A. Kurzman,[b] Ram Seshadri,[b] and Daniel E. Morse*[a]

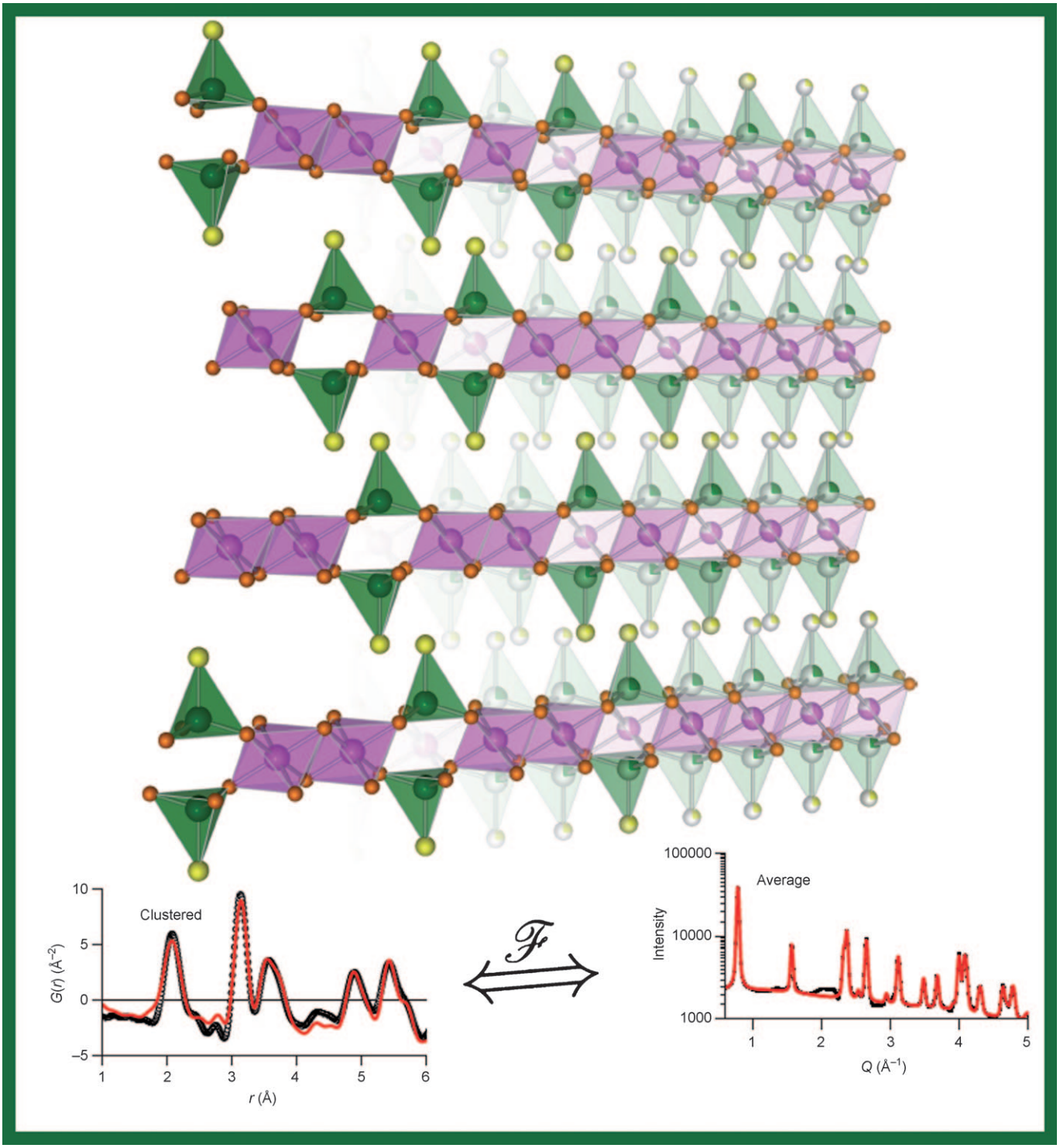

Abstract: Structures of layered metal hydroxides are not well described by traditional crystallography. Total scattering from a synthesis-controlled subset of these materials, as described here, reveals that different cobalt coordination polyhedra cluster within each layer on short length scales, offering new insights and approaches for understanding the properties of these and related layered materials. Structures related to that of brucite [$Mg(OH)_2$] are ubiquitous in the mineral world and offer a variety of useful functions ranging from catalysis and ion-exchange to sequestration and energy transduction, including applications in batteries. However, it has been difficult to resolve the atomic structure of these layered compounds because interlayer disorder disrupts the long-range periodicity necessary for diffraction-based structure determination. For this reason, traditional unit-cell-based descriptions have remained inaccurate. Here we apply, for the first time to such layered hydroxides, synchrotron X-ray total scattering methods—analyzing both the Bragg and diffuse components—to resolve the intralayer structure of three different α-cobalt hydroxides, revealing the nature and distribution of metal site coordination. The different compounds with incorporated chloride ions have been prepared with kinetic control of hydrolysis to yield different ratios of octahedrally and tetrahedrally coordinated cobalt ions within the layers, as confirmed by total scattering. Real-space analyses indicate local clustering of polyhedra within the layers, manifested in the weighted average of different ordered phases with fixed fractions of tetrahedrally coordinated cobalt sites. These results, hidden from an averaged unit-cell description, reveal new structural characteristics that are essential to understanding the origin of fundamental material properties such as color, anion exchange capacity, and magnetic behavior. Our results also provide further insights into the detailed mechanisms of aqueous hydrolysis chemistry of hydrated metal salts. We emphasize the power of the methods used here for establishing structure–property correlations in functional materials with related layered structures.

Keywords: cobalt · hydroxides · materials science · structure elucidation · synchrotron radiation · X-ray diffraction

Introduction

In many layered materials, weak interactions between layers results in a plethora of low-energy defects such as stacking faults.[1] These disrupt the three-dimensional periodicity of the system, making traditional diffraction studies difficult to perform.[2] While structural parameters, such as space group, lattice constants, and interlamellar separation, can be extracted from the observed broad and asymmetric Bragg peaks in the diffraction patterns, establishing the arrangements of atoms within the layers, as well as the nature and disposition of species between the layers is rather difficult. As an example, determining the arrangement of $Mg(OH)_6$ and $Al(OH)_6$ octahedra in the ubiquitous hydrotalcite mineral $[Mg_6Al_2(OH)_{16}][CO_3]\cdot 4H_2O$, a compound that serves as a model for a vast family of layered double hydroxides,[3] required the concurrent use of ^1H, ^{27}Al, and ^{25}Mg solid-state NMR techniques.[4] This problem had not been solved by decades of diffraction studies on these systems, because of negligible differences in scattering cross-sections of the different metal sites.[3]

The simplest layered hydroxides have the brucite $Mg(OH)_2$ structure, as in β-$Co(OH)_2$ depicted in Figure 1a. Replacement of one of the octahedrally coordinated divalent metal ions with a trivalent cation recruits an interlayer counteranion, such as CO_3^{2-} in the case of hydrotalcite or hydrotalcite-like compounds, shown in Figure 1b with Co^{2+} (pink) and Co^{3+} (black). With two distinct metal sites, these compounds are often referred to as layered double hydroxides; such materials play a large role in catalysis, geological ion exchange, and environmental mediation, yet the exact arrangement of atoms within each layer is still debated.[3] A subset of these materials, the layered hydroxide salts, formulated as $M^{2+}(OH)_{2-x}(A^{m-})_{x/m}\cdot n H_2O$,[5] contain only divalent metal ions. The lamellæ of these materials develop a positive charge from under-coordination or mixed coordination geometries of the intralayer cations. A prime example of this structure is α-$Co(OH)_2$, which can include a number of different counteranions.[6,7] Studies of cobalt hydroxide chloride have shown that the cobalt ions take on both octahedral and tetrahedral coordination geometries,[8] as portrayed in Figure 1c, and that changing the precursor hydrolysis rate in the synthesis process comprising hydrolysis and polycondensation varies the ratio of the different coordination arrangements, altering the structure within the layers.[9] Despite the many previous studies on the cobalt hydroxide chloride family, a detailed picture of the arrangement of metal sites, in terms of their coordination and distribution, has remained elusive. Even with high-resolution synchrotron

[a] J. R. Neilson, Prof. D. E. Morse
Interdisciplinary Graduate Program in
Biomolecular Science & Engineering
Institute for Collaborative Biotechnologies
Materials Research Laboratory, University of California
Santa Barbara, CA 93106-5160 (USA)
Fax: (+1) 805-893-8062
E-mail: d_morse@lifesci.ucsb.edu

[b] J. A. Kurzman, Prof. R. Seshadri
Materials Research Laboratory, University of California
Santa Barbara, CA 93106-5121 (USA)

Supporting information for this article is available on the WWW under http://dx.doi.org/10.1002/chem.201000661.

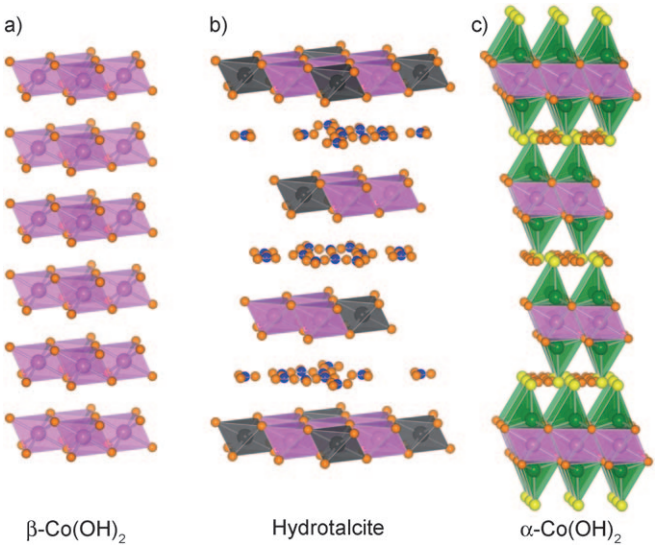

Figure 1. Schematic representations of β-$Co(OH)_2$, hydrotalcite, and α-$Co(OH)_2$ structures showing the different coordination states of divalent cobalt (pink: octahedral, green: tetrahedral), oxidation state (Co^{3+}: black), and lamellar separation. Orange spheres represent oxygen, blue: carbon, yellow: chlorine. Hydrogen omitted for clarity. The α-$Co(OH)_2$ structure has split-site occupancy between the metal atoms and the water positions. The depiction of α-$Co(OH)_2$ is highly averaged, with a high degree of partial occupancy.

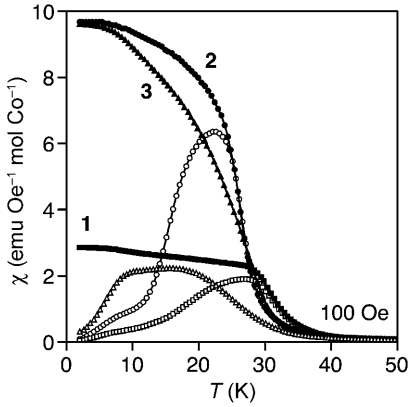

Figure 2. Magnetic susceptibility as a function of temperature from zero field cooling (open symbols) and field cooling (closed symbols) at 100 Oe for compounds **1** (squares), **2** (circles), and **3** (triangles) showing the distinct behavior of the three samples.

powder X-ray diffraction,[9] analysis of the data requires disordering through split atoms and partial occupancy (Figure 1c). Consequently, the positions of the two distinct metal ions are not spatially distinguished and their shared occupancy is statistically averaged over all metal sites, making an accurate description of all atom sites impossible using a traditional unit cell.

We focus here on three different cobalt hydroxide compounds, prepared by kinetic control of aqueous precursor hydrolysis, with different fractions of tetrahedrally coordinated cobalt ions (Co^{tet}), with **1** containing 40% Co^{tet}, **2** with 33% Co^{tet}, and **3** with 23% Co^{tet}, as previously described.[9] The use of the air–water interface to control the precipitation is an important aspect in the preparation, and all else being equal, provides highly ordered materials relative to materials produced by bulk precipitation.

Preliminary magnetic studies suggest that the metal sites (tetrahedral and octahedral) in these compounds are not arranged randomly. The magnetic susceptibility (Figure 2) of the three compounds is consistent with ferrimagnetic ordering, as determined from the different zero-field and field cooling temperature dependences. For **1** and **2**, multiple kinks in the χ versus T trace suggest distinct ordering tendencies within the different sublattices, and/or multiple magnetic transitions. Clearly, magnetic behavior in these compounds cannot be understood on the basis of average structural models such as the depiction used in Figure 1c.

Traditional diffraction studies define a periodic structure confined within a unit cell. In the materials presented here, this traditional structure description fails: these cobalt hydroxides have extensive site sharing of many atoms as a result of their disrupted three-dimensional periodicity, thus preventing an accurate description of all atom positions and occupancies. Here we use total scattering methods to analyze Bragg profiles and pair distribution functions of these materials.[10] The methods used here have been applied to numerous partially ordered systems including nanoparticles,[11] locally strained lattices,[12] and layered materials.[13–15] These methods also have been used to help explain poorly understood phenomena and properties.[16] We use these methods here to decouple different elements of static disorder and unravel the rules by which cation coordination and distribution are determined in α-$Co(OH)_2$.

Results and Discussion

Average structure from Rietveld analysis: The powder X-ray diffraction patterns of compounds **1**–**3** are shown on a log-scale in Figure 3a. All three samples share the same reflections, but display subtle differences in peak intensity and width, as well as distinct background profiles. Rietveld refinement of **2**, initialized with the rhombohedral structure described by Ma, et al.[8] is shown in Figure 4 and summarized in Table SI in the Supporting Information. The use of anisotropic thermal parameters significantly improves the fit, both visually (red difference curve, versus the isotropic difference in black; Figure 4) and statistically by decreasing R_{wp} from 5.5 to 5.0% and χ^2 from 5.5 to 4.6. Layered materials often have poor lamellar registry or turbostratic disorder that asymmetrically broaden diffraction peaks.[6] This, in addition to the diffuse scattering seen in the background profile, accounts for the relatively poor refinement statistics, although the quality of the fit appears excellent as judged visually. It is well known that refinement statistics are not the sole determinant of fit quality.[17]

The refined anisotropic thermal parameters indicate lamellar disorder, with the intralayer metal ions and bridg-

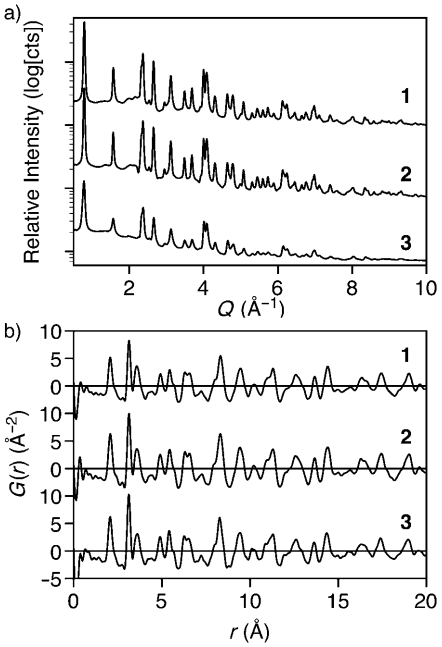

Figure 3. a) Synchrotron powder X-ray diffraction of samples **1** (top), **2** (middle), and **3** (bottom) in transmission showing similar Bragg profiles on a log scale with minor changes in relative peak intensities. b) Extracted pair distribution functions ($G(r)$) for samples **1** (top), **2** (middle), and **3** (bottom) showing identical peak positions for each sample with subtle variations in intensity.

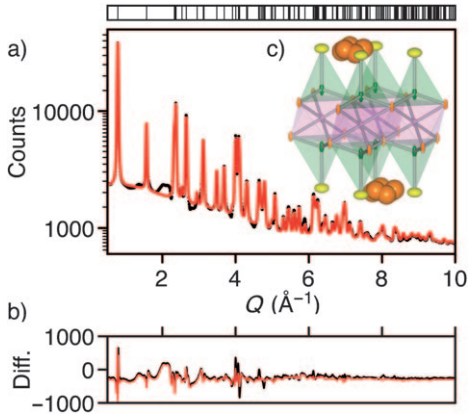

Figure 4. a) Rietveld refinement of sample **2** (black) with a calculated profile (red) using anisotropic thermal parameters. b) Difference curves illustrate a better fit with anisotropic thermal parameters (red) than with isotropic thermal parameters (black). Reflections are shown in the black ticks above the data. c) Structural representation of a layer within one unit cell of the split-atom structure showing ellipsoids of the anisotropic thermal parameters, implying increased out of plane disorder of bridging oxygen (orange) and cobalt (pink for Co^{oct}, green for Co^{tet}) atoms and generally disordered water. The chlorine atoms (yellow) show greater displacement in plane.

ing oxygen atoms exhibiting reduced in-plane displacements from U_{iso}, but enlarged U_{33} values, suggesting intralayer order and decoupling of the layers. Representation of the result by the thermal ellipsoids of one layer within a unit cell in Figure 4c illustrates this effect. Furthermore, the chlorine atoms show enlarged x–y atomic fluctuations, since the tetrahedral vertices are less topologically constrained in the ab plane and occupational disorder or site mixing with the water position could artificially increase the parameters. The water position is highly disordered, with a physically unrealistic thermal parameter ($U_{11}=0.1457$ Å^2) that is indicative of positional disorder rather than atomic displacement (Table SI in the Supporting Information).[10] Reduced lamellar correlations with anisotropic thermal parameters also have been observed in pair distribution function studies of disordered lamellar materials such as $V_2O_5{\cdot}n\,H_2O$ xerogels[13] and pyrolytic graphite.[18]

Each of the three samples exhibits various degrees of preparation-dependent paracrystallinity,[9] as seen in Figure 3a. Rietveld refinements for **1** and **3** are not stable when atom positions are refined. However, the decreasing fractional occupancy of Co^{tet} sites from **1** to **3** brings about a lattice contraction along the a axis (Table 1). As expected, the

Table 1. Summary of Rietveld refinement from compounds **1**, **2**, and **3** using isotropic thermal parameters.

Sample	a [Å]	c [Å]	R_{wp} [%]	R_p [%]	χ^2
1	3.14330(30)	24.0350(32)	7.26	4.89	11.40
2	3.14166(23)	24.0731(24)	5.51	3.80	5.52
3	3.1285(5)	24.228(6)	4.88	3.78	3.20

c axis expands with a axis contraction in order to retain the unit-cell density. Despite these reciprocal-space structural analyses, the intralayer structure of α-$Co(OH)_2$ remains elusive. As depicted in the split-atom structure shown in Figures 1 and 4c, two cobalt atoms may be only 1.7 Å apart; this would be closer than the cobalt–cobalt distance in metallic cobalt (≈2.5 Å), and thus chemically unreasonable, but not excluded by the average structure. While Rietveld analysis employing anisotropic thermal parameters (Figure 4c) reveals insights into the lamellar and positional disorder, the arrangement of metal sites remains unknown.

Local structure analysis using the pair distribution function: The experimentally extracted pair distribution functions (PDF) for **1**, **2**, and **3** (Figure 3b) are similar, but display subtle variations in intensity. We focus here mostly on the analysis of the PDF of **2**, and refer to the PDFs of **1** and **3** later. Shown in Figure 5, the experimental PDF of **2** (grey circles) is compared with the PDF simulated from the layered structures pictured in Figure 1. Refining scale factors and lattice parameters of the hydrotalcite $[Co^{2+}{}_6Co^{3+}{}_2(OH)_{16}][CO_3]{\cdot}4\,H_2O$[19] or of β-$Co(OH)_2$ structures yields poor fits to the data. The PDF profile for the average α-$Co(OH)_2$ structure is directly calculated from the structural parameters obtained by Rietveld refinement by using anisotropic thermal parameters. While the calculated profile describes the data at longer distances ($r \geq 5$ Å), the structural model only poorly fits the experimental data at short distances, even after accounting for correlated atomic displacements ($\delta_1 = 1.16$).[20] When the Rietveld refined isotropic

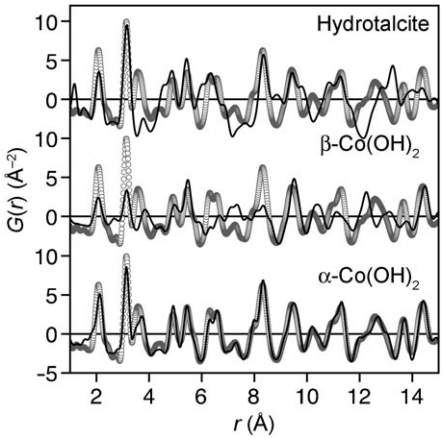

Figure 5. a) Pair distribution function of **2** with refined profiles of hydrotalcite and β-$Co(OH)_2$ and a calculated profile of α-$Co(OH)_2$ using anisotropic thermal parameters determined from Rietveld refinement, showing a reasonable fit at large distances, but under-representation of the local structure, even after accounting for correlated atomic displacements.

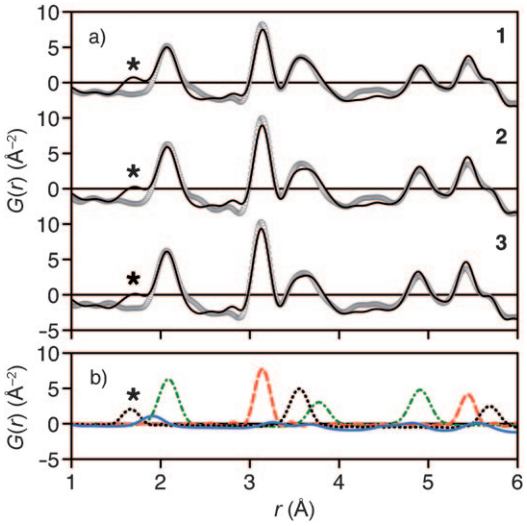

Figure 6. a) Pair distribution functions for each compound (grey circles), with refined average structures ($2.5 \le r \le 6$ Å; black lines), allowing g_{oct}, g_{water}, a, c, and the atom positions to change. The thermal parameters were equivalent for each refinement and all variables were sent successively from one refinement to the next. b) Deconvolution of the pair distribution function into major pair-wise contributions, Co^{tet}–O (solid blue line), Co^{oct}-O (dot-dashed green line), Co^{oct}–Co^{oct} (dashed red line), and Co^{oct}–Co^{tet} (dotted black line). The asterisk indicates the nearest neighbor Co^{oct}–Co^{tet} pairing, which is mandated by the average structure but distinctly not observed in the local structure, indicating that there are no tetrahedral cobalt sites directly capping octahedral cobalt.

thermal parameters are used (data not shown), the fit is worse at short distances, indicative of anisotropic local order, such as the intralayer order depicted in Figure 4c, with $U_{11} < U_{33}$ for the intralayer species. This trend is consistent with the PDFs for **1** and **3**. In fact, the major differences in $G(r)$ between the three materials (**1**–**3**) are systematically modulated peak intensities below 6 Å.

Peak intensities of the pair distribution function calculated from the average structure are strongly influenced by the occupancy of the split-atom sites ($g_{Co(1)}$, $g_{Co(2)}$, g_{Cl}, $g_{O(2)}$) and all atomic displacement parameters. The large anisotropic thermal parameters masquerading for static disorder in the Rietveld analysis are not required in the PDF analysis of short-range atomic correlations within a layer. A range-dependent real-space refinement links the reduced intensity of pair-wise correlations at high r with increased atomic displacement parameters, as in the case of layered $V_2O_5{\cdot}n\,H_2O$[13] or exfoliated titanate nanosheets[15] (Supporting Information, Figure S3 and Table SII). A similar but invariant analysis performed on powdered nickel metal (Supporting Information, Figure S4 and Table SIII) excludes contributions from instrumental broadening at increased r.[21] Therefore, an independent analysis of the short-range PDF ($r < 6$ Å) describes details of intralayer atomic arrangements without the convolution with extended static disorder.

Local metal site coordination: Since the average structure describes many of the features of $G(r)$ accurately, it was refined over short distances to quantify the ratio of six- to four-coordinate cobalt sites. These results are summarized in Figure 6, Table 2, and Table SIV in the Supporting Information. Beginning with the PDF for compound **1**, the average structure from Rietveld refinement (Table SI in the Supporting Information) was refined in real space from 2.5 to 6 Å, allowing all parameters to change concomitant to the $R\bar{3}m$ space group (Figure 6a). Since the occupancies and thermal parameters are convoluted, the variable occupancies ($g_{Co(1)}$, $g_{O(2)}$) were initially held constant from the Rietveld refinement, allowing the atomic displacement coefficients to converge, along with a coefficient describing correlated atomic displacements. The linked occupancies ($g_{Co(2)} = g_{Cl} = 1 - g_{Co(1)}$) were then allowed to co-refine with the atom positions and lattice constants and are reported in the Supporting Information (Table SIV). Hydrogen (hydroxyl and water bound) is included in the refinement in order to accurately represent the average number density (ρ_0), but neither its position nor thermal displacement is refined.

Table 2. Summary of real-space refinements of the pair distribution functions for **1**, **2**, and **3**, using the disordered average structure.

Sample	a [Å]	c [Å]	Co^{tet} [%]	R_w [%]
1	3.14155(6)	24.165(5)	33.8	21.7
2	3.13677(7)	24.267(45)	26.6	20.3
3	3.12727(1)	24.2704(72)	24.9	18.8

For compounds **2** and **3**, the atom positions and thermal parameters were constrained from the analysis of **1**, while the lattice parameters and occupancies varied (Figure 6a). The refinement was only run from 2.5 to 6 Å, because of an evident discrepancy in the data at ≈1.7 Å indicated by an asterisk. Deconvolution of the PDF into individual pair-wise contributions, shown in Figure 6b, reveals that the calculated PDF peak at 1.7 Å results from a Co^{oct}–Co^{tet} correlation. This feature is not observed in the experimental $G(r)$ for any compound (**1**–**3**), meaning that a four-coordinate cobalt

ion cannot sit on top of a six-coordinate cobalt ion, as depicted in Figure 4c or Figure 1. While this result has been previously assumed,[8,9] this is the first structural observation in α-$Co(OH)_2$ showing that the tetrahedrally coordinated cobalt sites require an octahedral vacancy in the layer.

Deconvolution of the calculated $G(r)$, Figure 6b, illustrates that the PDF peaks at 3.1 and 5.4 Å result from Co^{oct}–Co^{oct} pair-wise correlations. The added intensity of these peaks from **1** to **3** reflects the increased Co^{oct} in the lattice as determined analytically. Correspondingly, the peak at 3.6 Å, derived from Co^{oct}–Co^{tet} pairing (Figure 6b), consistently decreases in intensity from **1** to **3** with the analytically measured fraction of Co^{tet} sites, based on the assumption of one chloride anion per tetrahedral vertex. Quantitative refinement of the occupancy of tetrahedral sites in the lattice, $1-g_{Co(1)}$, decreases from compound **1** to **3** (Table 2). The refined values of the occupancy are consistent with the assumed occupancies derived from analytical measurements of the chloride concentration (ICP and EDS),[9] despite their convolution with thermal displacement parameters. In support of this observation, the planar lattice parameter, *a,* contracts from **1** to **3** (Table 2), as also observed from Rietveld refinement (Table 1). As the cation concentration per layer increases from the replacement of a Co^{oct} vacancy with two Co^{tet} sites, enhanced cation–cation repulsion within the layer expands the lattice in the *ab* plane. Regardless of the absolute occupancies, this analysis unequivocally shows that the kinetically controlled hydrolytic synthesis controls the distribution of intralayer metal coordination of the layered hydroxide, as previously described,[9] and the pair distribution function analysis provides a quantitative comparison.

Local metal site distribution: While a quantitative description of the metal coordination geometry with the average structure is important, it does not accurately describe the local distribution of metal sites, as evident from the anomalous peak at 1.7 Å in Figure 6a. Therefore, we model three different structures with specific ordering of the metal polyhedra within the layer. A schematic layer of each of the three calculated structures, in comparison with the split-atom average structure, is illustrated in Figure 7. The structures labeled $[(Co^{oct})_3(Co^{tet})_2]$, $[(Co^{oct})_8(Co^{tet})_2]$, and $[(Co^{oct})_{15}(Co^{tet})_2]$, with a linear connectivity of one, two, and three octahedral cobalt sites between tetrahedrally coordinated cobalt sites, have 40% Co^{tet}, 20% Co^{tet}, and 12% Co^{tet}, respectively. These structures are necessarily generated using *P*1 symmetry in order to retain the same relative atom positions, displacements, and stacking sequence as the disordered average structure determined from Rietveld analysis (Tables SII and SIV in the Supporting Information). There is no evidence of long-range periodicity of the ordered phases observed in the Bragg profiles shown in Figure 3, which would lift the split-atom degeneracy, as in the case of the analogous zinc mineral, $Zn_5(OH)_8(Cl)_2(H_2O)$, Simonkolleite.[22] All three structures generally describe the experimental pair distribution function at longer real space distances, indicative of an accurate representation

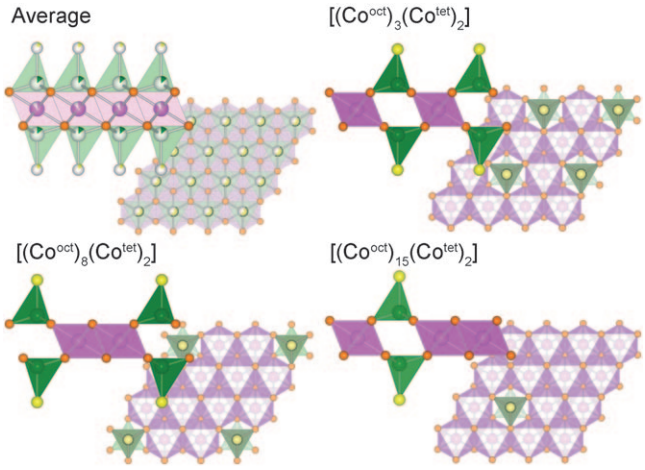

Figure 7. Structural models containing different distributions of metal polyhedra, with a random site distribution (Average), one Co^{oct} site (pink) between Co^{tet} sites (green) $[(Co^{oct})_3(Co^{tet})_2]$, two Co^{oct} sites between Co^{tet} $[(Co^{oct})_8(Co^{tet})_2]$, and a connectivity of three Co^{oct} sites between Co^{tet} $[(Co^{oct})_{15}(Co^{tet})_2]$, showing the linear in-plane separation (*a*-axis, front) and planar distribution (*c* axis, back). Fractionally shaded atoms (average model) indicate split-site occupancies. Oxygen atoms depicted in orange, chlorine in yellow. Hydrogen and water positions omitted for clarity.

of the stacking sequence and overall lattice connectivity (Figure 8, $r>6$ Å). Locally, with $r<6$ Å, only the $[(Co^{oct})_8(Co^{tet})_2]$ structure accounts for the intensity of the PDF for compound **2**. While this structure does not describe the reciprocal-space structure and Bragg profile, we conclude that there is short-range ordering within the layer that has an ordered distribution of polyhedra like the $[(Co^{oct})_8(Co^{tet})_2]$ structure, with a linear connectivity of two Co^{oct} sites between Co^{tet} sites.

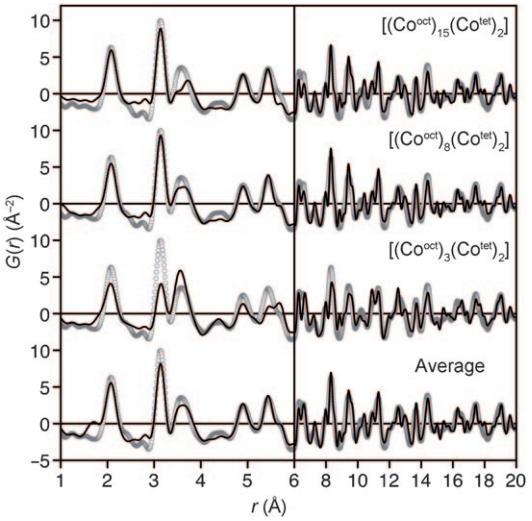

Figure 8. Pair distribution function for **2** with calculated structural models containing different polyhedral distributions, in comparison with the site-disordered average structure. The best short range fit is observed with the $[(Co^{oct})_8(Co^{tet})_2]$ local geometry, whereas all structures describe the extended structure reasonable well ($r>6$ Å).

Since there is no evidence from Rietveld analysis for the $[(Co^{oct})_8(Co^{tet})_2]$ phase, we simulated a weighted average of the three ordered phases described above in order to provide a representation consistent with the average structure. Weighted averages of locally ordered phases are often used to describe atomic positions of different alloys for which supercell reflections are not observed, but the local structure is indicative of structural heterogeneity, as in the case of alloy induced lattice strain of $In_{1-x}Ga_xAs$[12] or $CoAl_{2-x}Ga_xO_4$.[23] The experimental PDF is fit with the weighted average of the three ordered phases shown in Figure 7, after refinement of only the scale factors (Table 3).

Table 3. Summary of real-space refinements of the pair distribution functions for **1**, **2**, and **3**, using a locally ordered multiple-phase fit.

Sample	A[a]	B[a]	C[a]	Co^{tet} [%]	R_w [%]
1	35.9	49.1	15.0	26.0	21.9
2	28.6	50.9	20.5	24.0	23.1
3	22.2	47.2	30.6	21.9	22.9

[a] A, B, and C correspond to the atomic phase fractions of $[(Co^{oct})_3(Co^{tet})_2]$, $[(Co^{oct})_8(Co^{tet})_2]$, and $[(Co^{oct})_{15}(Co^{tet})_2]$ ordered phases, respectively, calculated from the scaling factors, which were not constrained to a sum of 100%.

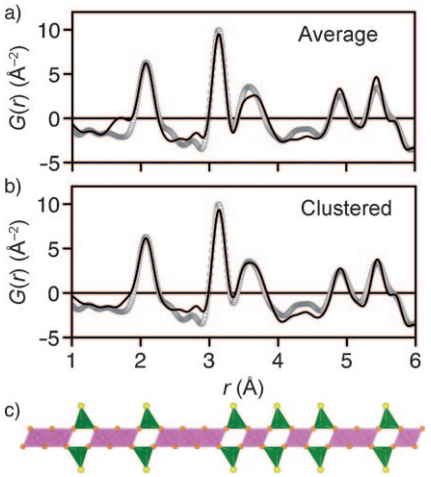

Figure 9. Pair distribution function for **2** (grey circles) with a) a calculated average structure containing an equivalent number of tetrahedrally coordinated cobalt ions (black line) as b) from refining scaling factors of a three-phase material with $[(Co^{oct})_3(Co^{tet})_2]$, $[(Co^{oct})_8(Co^{tet})_2]$, and $[(Co^{oct})_{15}(Co^{tet})_2]$ clustered phases (black line), all other things being equal, in order to illustrate the effect of cation site distribution and clustering within the layer. c) Schematic atomic representation of one layer showing short-range clustering of the three different types of coexistent ordered phases. Cobalt atoms shown in pink (six-coordinate) and green (four-coordinate), oxygen in orange, and chlorine in yellow. Hydrogen and water positions omitted for clarity.

Furthermore, the sum of the scale factors is not constrained to 1, providing an objective result. We repeat this analysis for all three synthesized compounds (**1**–**3**) and calculate the relative atomic fractions of each phase from the scale factors to arrive at a quantitative number of tetrahedrally coordinated cobalt atoms in the overall material for each compound (Table 3). Using these ratios to determine site occupancy, we also report the equivalent $G(r)$ for the disordered average structure, as shown in Figure 9a for **2**. The clustered, or weighted average, model is displayed in Figure 9b. The calculations for **1** and **3** are presented in the Supplementary Information, Figure S5, and the results are summarized in Table 3. This analysis allows an independent comparison of the effect of the distribution of metal sites within the lattice, all other things being equal.

The subtle differences between the two calculated profiles in Figure 9 reveal important and newly recognized features of the intralayer structure. The anomalous peak at 1.7 Å in the average structure does not represent the data, but is resolved with the clustered model, which specifically introduces two Co^{tet} sites sandwiching a Co^{oct} vacancy. Another discrepancy is the peak in the average structure at 3.6 Å, corresponding to Co^{oct}–Co^{tet} pair-wise correlations (Figure 6b). The disordered distribution of polyhedra does not capture all of the intensity of the 3.6 Å peak (Figure 9a). The well-described intensity of the 3.6 Å peak for **2** from the clustered model (Figure 9b) results from incorporation of the $[(Co^{oct})_3(Co^{tet})_2]$ phase (26.7 at%), which has the most Co^{oct}–Co^{tet} correlations. Alternatively, the poor fit of the disordered model can structurally manifest in a hypothetical, but allowed, local arrangement in which a Co^{tet} site studs only one side of the layer either above or below a Co^{oct} site, reducing the number of Co^{oct}–Co^{tet} correlations for a fixed number of Co^{tet} sites. The clustered model is also supported by the better representation of the next-nearest Co^{oct} neighbor peak at 5.4 Å. In the $[(Co^{oct})_3(Co^{tet})_2]$ phase, there are correspondingly fewer next-nearest-neighbor correlations at 5.4 Å relative to the disordered structure with an equal number of Co^{tet} sites (Figure S6 in the Supporting Information), because a tetrahedrally coordinated cobalt is present in every-other metal site, as observed when projected along the *c* axis (Figure 7).

The overall ratio of Co^{tet} is compensated by an increasing fraction of $[(Co^{oct})_{15}(Co^{tet})_2]$ from **1**–**3**, and a decreasing fraction of $[(Co^{oct})_3(Co^{tet})_2]$ from **1**–**3**, while the $[(Co^{oct})_8(Co^{tet})_2]$ phase does not vary systematically with composition, as summarized in Table 3. The short range of this analysis ($1 < r < 6$ Å) assures that solely intralayer pair-wise interactions are modeled, but the long-range calculated structures (Figure 8, $r > 6$ Å) show no gross misrepresentation of peak locations or intensities. Therefore, a schematic representation of the local structure may appear as depicted in Figure 9c, in which each of the different ordered phases is included within a layer according to the atomically weighted scale factors. Randomly distributed clusters, with coherence lengths less than a few unit cells, would also generate the observed split-atom average structure determined from Rietveld refinement of the Bragg profile.

Only with total scattering analysis, of both Bragg and diffuse scattering profiles, can the atom positions of these lamellar structures be accurately described. Furthermore, the evidence of intralayer clustering as depicted in Figure 9c,

aids in the explanation of the unusual magnetic behavior shown in Figure 2. Additional analysis with low-temperature total neutron scattering of analogous cobalt deuteroxides is underway to help further understand the local, average, and magnetic structures of α-$Co(OH)_2$ structures. With well-defined atom positions, excluding interlayer water, the distribution and occupancy of the metal sites clearly depend on the length scale at which they are examined: local analysis provides evidence of randomly distributed intralayer clusters, which consistently gives the average appearance of randomly split metal site occupancies over extended length scales.

Conclusion

Despite the prevalence of static disorder in α-$Co(OH)_2$, both in a preparation-dependent and a length-scale dependent manner, local structural characteristics are obeyed. While α-$Co(OH)_2$ structures have been described for several decades, the precise arrangement of atoms within the defect brucite layers has remained elusive. Here we have observed and summarized various rules regarding the atom positions and occupancies in the α-$Co(OH)_2$ family, as determined from structural analysis at multiple length scales. The average structure is incomplete; all metal sites and water positions require split-site occupancies due to an absence of long-range ordering of tetrahedrally coordinated cobalt within the layers. Each brucite-like layer has well-defined atom positions, but poor coupling between the layers, as supported by both real- and reciprocal-space analyses. Furthermore, the local pair distribution function is better described by a weighted average of different phases consisting of symmetrically distributed metal polyhedra rather than a random distribution of metal polyhedra on average. This offers significant new insights into the connectivity and clustering of metal polyhedra within the layers and opens up the interpretation of previously reported Bragg patterns based on a traditional unit cell description of the atom positions. We anticipate that the results presented here will point the way to understanding myriad related compounds, and will help address important questions regarding structural chemistry and related physical properties.

Experimental Section

We employed kinetically controlled aqueous hydrolysis of a molecular precursor, as previously described,[24] to prepare three compounds: $Co_{1.25}(OH)_2(Cl)_{0.5}(H_2O)_{0.4}$ (**1**), $Co_{1.20}(OH)_2(Cl)_{0.40}(H_2O)_{1.1}$ (**2**), and $Co_{1.13}(OH)_2(Cl)_{0.26}(H_2O)_{1.5}$ (**3**), the chemical compositions of which have been previously analyzed by inductively coupled plasma atomic emission spectroscopy (ICP) and energy dispersive spectroscopy (EDS).[9] The compounds were prepared from aqueous cobalt chloride (0.1 M) at the air–water interface by using 1.2, 0.6, and 12% $NH_{3(aq)}$ (v/v) solutions as the volatile hydrolytic catalyst to obtain **1**, **2**, and **3**, respectively. Separation of the material from the solution by use of the Langmuir–Blodgett technique ensures that only product formed by kinetic control is isolated. The fractions of tetrahedrally coordinated cobalt were approximated from the stoichiometric ratios of incorporated chloride by assuming one chloride ion per tetrahedral cobalt, such that **1** contains 40% of four-coordinate cobalt ions (Co^{tet}), **2** with 33% Co^{tet}, and **3** with 23% Co^{tet}. Samples were ground into a fine powder for subsequent investigations using an agate mortar and pestle and stored in sealed containers. Magnetic susceptibility measurements were performed on powders immobilized in paraffin wax using a Quantum Designs MPMS 5XL SQUID magnetometer.

Synchrotron XRD (X-ray diffraction) data were collected at room temperature, in transmission on beamline 11-ID-B at the Advanced Photon Source, Argonne National Laboratory, with an X-ray energy of about 90 keV. Powder samples were loaded into Kapton tubes and placed vertically in a sample holder in the path of the beam, with an experimental set-up similar to that described by Chupas et al.[25] Scattering data were collected on an amorphous silicon detector from General Electric Healthcare at sample-to-detector distances of 650 mm (Rietveld) and around 140 mm (pair distribution function). The data were processed using the program FIT2D[26] to yield the corresponding one-dimensional XRD pattern, accounting for beam polarization. The pair distribution function (PDF), $G(r)=4\pi r[\rho(r)-\rho_0]$,[10,27] was extracted with the program PDFgetX2,[28] using a maximum momentum transfer of $Q_{max}=25$ Å^{-1}. Bulk cubic CeO_2 was used to calibrate the sample to detector distance, and for constructing an instrument parameter file for refinements in GSAS,[29] with instrument parameters (Q-damp and Q-broad) for PDF analysis obtained by refining a PDF of Ni powder. Full structure profile refinements with the PDF data were carried out in the program PDFFIT2 and PDFgui.[20,30] Specific refinement recipes are described in detail throughout the text. Structural models are rendered using VESTA.[31]

Acknowledgements

This research and D.E.M. were supported by a grant from the U.S. Department of Energy Office of Basic Energy Sciences (DEFG03-02ER46006). Use of the Advanced Photon Source was supported by the U.S. Department of Energy, Office of Basic Energy Sciences, under Contract No. DE-AC02-06CH11357. Additional instrumentation was provided by the UCSB Materials Research Laboratory (supported by award No. DMR05-20415) from the U.S. National Science Foundation MRSEC Program. J.R.N. thanks the National Science Foundation for support through a Graduate Research Fellowship. We thank Peter J. Chupas, Evan R. Maxey of the APS and Serena Corr of the UCSB Materials Research Laboratory for assistance with collection and processing of synchrotron data and B. Schwenzer, B. C. Melot, and D. P. Shoemaker for their excellent advice.

[1] A. F. Wells, *Structural Inorganic Chemistry*; Clarendon Press, Oxford, **1984**.
[2] A. Radha, P. Kamath, C. Shivakumara, *Acta Crystallogr. Sect. B* **2007**, *63*, 243–250.
[3] V. Rives, *Layered Double Hydroxides: Present and Future*, Nova, New York, **2001**.
[4] P. J. Sideris, U. G. Nielsen, Z. Gan, C. P. Grey, *Science* **2008**, *321*, 113–117.
[5] G. Arizaga, K. Satyanarayana, F. Wypych, *Solid State Ionics* **2007**, *178*, 1143–1162.
[6] M. Rajamathi, P. V. Kamath, R. Seshadri, *Mater. Res. Bull.* **2000**, *35*, 271–278.
[7] Y. Du, D. O'Hare, *J. Phys. Chem. Solids* **2008**, *69*, 1040–1043.
[8] R. Ma, Z. Liu, K. Takada, K. Fukuda, Y. Ebina, Y. Bando, T. Sasaki, *Inorg. Chem.* **2006**, *45*, 3964–3969.
[9] J. Neilson, B. Schwenzer, R. Seshadri, D. Morse, *Inorg. Chem.* **2009**, *48*, 11017–11023.
[10] T. Egami, S. Billinge, *Underneath The Bragg Peaks: Structural Analysis of Complex Materials, Vol. 7*, Pergamon Press, Oxford, **2003**.

[11] M. B. Smith, K. Page, T. Siegrist, P. L. Redmond, E. C. Walter, R. Seshadri, L. E. Brus, M. L. Steigerwald, *J. Am. Chem. Soc.* **2008**, *130*, 6955–6963.
[12] I.-K. Jeong, F. Mohiuddin-Jacobs, V. Petkov, S. J. L. Billinge, S. Kycia, *Phys. Rev. B* **2001**, *63*, 205–202.
[13] V. Petkov, P. Trikalitis, E. Bozin, S. Billinge, T. Vogt, M. Kanatzidis, *J. Am. Chem. Soc.* **2002**, *124*, 10157–10162.
[14] V. Petkov, S. Billinge, J. Heising, M. Kanatzidis, *J. Am. Chem. Soc.* **2000**, *122*, 11571–11576.
[15] M. Gateshki, S. Hwang, D. Park, Y. Ren, V. Petkov, *Chem. Mater.* **2004**, *16*, 5153–5157.
[16] K. Page, T. Kolodiazhnyi, T. Proffen, A. Cheetham, *Phys. Rev. Lett.* **2008**, *101*, 205502.
[17] B. Toby, *Powder Diffr.* **2006**, *21*, 67.
[18] V. Petkov, R. G. Difrancesco, S. J. L. Billinge, M. Acharya, H. C. Foley, *Philos. Mag. B* **1999**, *79*, 1519–1530.
[19] "Structural Aspects of Layered Double Hydroxides": D. G. Evans, R. C. T. Slade in *Layered Double Hydroxides*, Springer, Berlin, **2006**, p. 187.
[20] a) T. Proffen, S. J. L. Billinge, *J. Appl. Crystallogr.* **1999**, *32*, 572–575; b) I.-K. Jeong, R. H. Heffner, M. J. Graf, *Phys. Rev. B* **2003**, *67*, 104301.
[21] X. Qiu, E. Bozin, P. Juhas, T. Proffen, S. Billinge, *J. Appl. Crystallogr.* **2004**, *37*, 110–116.
[22] F. Hawthorne, E. Sokolova, *Can. Mineral.* **2002**, *40*, 939–946.
[23] B. C. Melot, K. Page, R. Seshadri, E. M. Stoudenmire, L. Balents, D. L. Bergman, T. Proffen, *Phys. Rev. B* **2009**, *80*, 104420.
[24] B. Schwenzer, K. M. Roth, J. R. Gomm, M. Murr, D. E. Morse, *J. Mater. Chem.* **2006**, *16*, 401–407.
[25] P. Chupas, X. Qiu, J. Hanson, P. Lee, C. Grey, S. Billinge, *J. Appl. Crystallogr.* **2003**, *36*, 1342–1347.
[26] A. Hammersley, S. Svensson, M. Hanfland, A. Fitch, D. Hausermann, *High Pressure Res.* **1996**, *14*, 235–248.
[27] B. Cullity, S. Stock, *Elements of X-ray Diffraction*, 3rd ed., Prentice Hall, Upper Saddle River, **2001**.
[28] C. L. Farrow, P. Juhas, J. W. Liu, D. Bryndin, E. S. Bozin, J. Bloch, T. Proffen, S. J. L. Billinge, *J. Phys. Condens. Matter* **2007**, *19*, 335219.
[29] X. Qiu, J. W. Thompson, S. J. L. Billinge, *J. Appl. Crystallogr.* **2004**, *37*, 678.
[30] A. C. Larson, R. B. V. Dreele, Los Alamos National Laboratory Report LAUR, **2000**, 86748.
[31] K. Mommas, F. Izumi, *J. Appl. Crystallogr.* **2008**, *41*, 653–658.

Received: March 16, 2010
Published online: August 2, 2010

